

Prediction of the Optical Polarization and High Field Hyperfine Structure Via a Parametrized Crystal-Field Model for the Low Symmetry Centers in Er^{3+} Doped Y_2SiO_5

N. L. Jobbitt,^{1,2} J.-P. R. Wells,^{1,2,*} M. F. Reid,^{1,2,†} S. P. Horvath,³ P. Goldner,⁴ and A. Ferrier^{4,5}

¹*School of Physical and Chemical Sciences, University of Canterbury, PB4800 Christchurch 8140, New Zealand*

²*The Dodd-Walls Centre for Photonic and Quantum Technologies, New Zealand*

³*Department of Electrical Engineering, Princeton University, Princeton, NJ 08544, USA*

⁴*Chimie ParisTech, PSL University, CNRS, Institut de Recherche de Chimie Paris, 75005 Paris, France*

⁵*Faculté des Sciences et Ingénierie, Sorbonne Université, UFR 933, 75005 Paris, France*

(Dated: June 22, 2022)

We report on the development and application of a parametrized crystal-field model for both C_1 symmetry centers in trivalent erbium-doped Y_2SiO_5 . High resolution Zeeman and temperature dependent absorption spectroscopy was performed to acquire the necessary experimental data. The obtained data, in addition to the ground ($^4I_{15/2}Z_1$) state and excited ($^4I_{13/2}Y_1$) state Zeeman and hyperfine structure, was simultaneously fitted in order to refine an existing crystal-field interpretation of the $\text{Er}^{3+}:\text{Y}_2\text{SiO}_5$ system. We demonstrate that it is possible to account for the electronic, magnetic and hyperfine structure of the full $4f^{11}$ configuration of $\text{Er}^{3+}:\text{Y}_2\text{SiO}_5$ and further, that it is possible to predict both optical polarization behavior and high magnetic field hyperfine structure of transitions in the $1.5 \mu\text{m}$ telecommunications band.

I. INTRODUCTION

The last two decades have seen a global interest in the development of quantum information storage and communication devices in order to enhance the current classical computation and communication infrastructure [1]. Progress in this field has provided demonstrations of optical quantum memories, quantum gate implementations and single-photon sources [2–8]. Recently, demonstrations have been made showing control of multiple ions at the single-photon level [9]. Lanthanide-doped Y_2SiO_5 is an ideal material for the realization of such devices owing to the small nuclear moment of yttrium and low abundance of Si and O isotopes with non-zero nuclear spin [10, 11]. A direct consequence of this is the possibility of long storage times for information encoded into a qubit [12]. This has enabled the observation of coherence times of over 1 min for $\text{Pr}^{3+}:\text{Y}_2\text{SiO}_5$; while $\text{Eu}^{3+}:\text{Y}_2\text{SiO}_5$ has exhibited a coherence time of over 6 h [4, 13]. The key technique used in order to obtain these coherence times is the zero-first-order-Zeeman (ZEFOZ) technique. This technique involves determining external magnetic field strengths at which the electronic structure of the system is insensitive to small fluctuations of the magnetic field in any direction. The field points at which this occurs are known as ZEFOZ points, which are avoided crossings of the hyperfine levels that exist in lanthanide-doped materials. At these points the dephasing induced by spin flips on neighboring host lattice ions is minimized, resulting in the long observed coherence times. As ZEFOZ points are located within the complex hyperfine structure of lanthanide-doped crystals, they have proven diffi-

cult to find experimentally, however, ZEFOZ points can be computationally predicted through the use of a spin Hamiltonian [14]. The key advantage in using a spin Hamiltonian is that it more accurately models the magnetic and hyperfine structure of an individual state when compared to its crystal-field theory counterparts. When combined with a crystal-field model, which aims to reproduce the entire electronic configuration, a unique set of parameters can be obtained which then can be easily transferred between ions within the lanthanide series.

Trivalent erbium is of particular interest for quantum information applications as the ion possesses optical transitions in the well established $1.5 \mu\text{m}$ telecommunications band, the narrowest optical homogeneous linewidth observed to date (50 Hz) [15], in addition to a spin coherence time of over one second [5]. Furthermore, Er^{3+} has a large hyperfine splitting relative to Pr^{3+} and Eu^{3+} [4, 13, 16] which allows for larger memory bandwidths within these hyperfine transitions while still obtaining reasonably long coherence times.

Recently, crystal-field analyses have been performed for the C_1 symmetry centers in Ce^{3+} , Er^{3+} and Yb^{3+} doped Y_2SiO_5 [16–19]; with further analyses under way for Y_2SiO_5 doped with Nd^{3+} , Sm^{3+} and Ho^{3+} [20–22].

We report on infrared to visible Zeeman absorption spectroscopy for both Er^{3+} centers in Y_2SiO_5 , the data from which culminates in a parametrized crystal-field model accounting for the energy level structure up to $27\,000 \text{ cm}^{-1}$, approximately seventy electronic g values measured along all three crystallographic axes as well as electron-paramagnetic resonance and Raman-heterodyne measurements obtained from the literature [16, 23–25]. The directional data provided by our Zeeman measurements over tens of electronic levels, allows us to obtain a well determined, unique set of crystal-field parameters and therefore goes well beyond what has been reported

* jon-paul.wells@canterbury.ac.nz

† mike.reid@canterbury.ac.nz

previously. We demonstrate that, from this analysis, we can account for high magnetic-field hyperfine splittings as well as the optical polarization behavior in this technologically important material.

II. EXPERIMENTAL

Y_2SiO_5 is a monoclinic silicate crystal with C_{2h}^6 space group symmetry and lattice constants; $a = 10.4103 \text{ \AA}$, $b = 6.7212 \text{ \AA}$, $c = 12.4905 \text{ \AA}$, and $\beta = 102^\circ 39'$ [26]. Here the crystallographic b axis corresponds to the C_2 rotation axis and the crystallographic a and c axes are located in the mirror plane which is perpendicular to the crystallographic b axis. Following the convention of Li *et al.* we define the optical extinction axes as D_1 and D_2 which are located in the a - b mirror plane and are perpendicular to each other in addition to the b axis [27]. In this study we focus on the X_2 phase of Y_2SiO_5 , which has two substitutional Y^{3+} sites, denoted as site 1 and site 2. Both of these sites have C_1 symmetry and here we follow the assignments made by [28]. Additionally, each site of Y_2SiO_5 also contains two magnetically inequivalent orientations, related by a 180° rotational symmetry, which arises from the C_{2h} symmetry of the unit cell. This is particularly relevant in terms of Zeeman studies as the two orientations respond differently when a magnetic field is applied outside of the D_1 - D_2 plane or the b axis [24].

The sample used in this study was grown in the X_2 phase of Y_2SiO_5 using the Czochralski process with an Er^{3+} dopant concentration of 0.005 molar %. The sample was grown to include natural abundances of erbium, of which ^{167}Er is the only isotope to have a nuclear spin, with $I = 7/2$. The crystal has dimensions of 6.27 mm along the D_1 axis, 6.18 mm along the D_2 axis, and 4.89 mm along the crystallographic b axis.

High resolution temperature dependent and Zeeman spectroscopy was performed using a Bruker Vertex 80 Fourier transform infrared (FTIR) spectrometer, operated at a resolution of 0.1 cm^{-1} . Temperature dependent spectroscopy was performed by mounting the crystal on a copper holder and was cooled by thermal contact with a closed-cycle helium cryostat. The sample temperature was controlled by a temperature controller which adjusted the current through a resistive heater attached to the back of the sample cold finger.

Zeeman spectroscopy was performed by attaching the sample to a copper mount which was then screwed into the bore of a 4 T Oxford Instruments superconducting solenoid built into a liquid helium cryostat.

III. RESULTS AND DISCUSSION

The $4f^{11}$ configuration appropriate to Er^{3+} has 182 doubly degenerate Kramers states, split into 41 multiplets. ^{167}Er is the only naturally occurring isotope of erbium to have a non-zero nuclear spin, with $I = 7/2$.

A. Temperature dependent absorption spectroscopy

Previously, the crystal-field electronic energy levels of both sites in $\text{Er}^{3+}:\text{Y}_2\text{SiO}_5$ have been measured, and reported, up to the $^2\text{H}_{11/2}$ multiplet at $20\,000 \text{ cm}^{-1}$ [23]. We extend this work to $27\,000 \text{ cm}^{-1}$ to include the $^4\text{F}_{7/2}$, $^4\text{F}_{5/2}$, $^2\text{H}_{9/2}$ and $^4\text{G}_{11/2}$ multiplets through the use of high resolution temperature dependent absorption spectroscopy.

Fig. 1 presents the 12 K absorption spectra of most excited multiplets up to the $^4\text{G}_{11/2}$ multiplet of $\text{Y}_2\text{SiO}_5:0.005\%\text{Er}^{3+}$ with all transitions assigned, with the exception of the $^4\text{F}_{3/2}$ multiplet and two levels of the $^2\text{H}_{9/2}$ multiplet for site 1 which were too weak to be observed. Levels were assigned to their respective sites by monitoring transitions from the excited states in the ground multiplet (hot lines) as the sample temperature was increased to 100 K. The 100 K spectra are omitted for brevity. The thermal population of states up to the $^4\text{I}_{15/2}\text{Z}_4$ state for both sites is evident at temperatures as low as 100 K. As the two sites of $\text{Er}^{3+}:\text{Y}_2\text{SiO}_5$ have an electronic energy level structure that are distinct from each other, each site therefore has a unique pattern which can be used to assign each spectral line found in absorption. Transitions from the $^4\text{I}_{15/2}\text{Z}_1$ state to their respective excited states are labeled as either belonging to site 1 or site 2 with a subscript. The spectral features labeled with an overbar are transitions from the $^4\text{I}_{15/2}\text{Z}_2$ state to the excited states. The extra structure seen in the $6\,700 - 6\,900 \text{ cm}^{-1}$ range of the $^4\text{I}_{13/2}$ multiplet is absorption due to residual atmospheric water vapor. Spectral features that could not be assigned as belonging to Er^{3+} are marked with an ‘*’.

With the inclusion of this additional data, a total of 51 and 53 electronic states are assigned for site 1 and site 2 respectively. These values are summarized in Tables I and II respectively. With absorption to all multiplets remeasured here except the ground multiplet. The assignments made by Doualan *et al.* were used for these states in the crystal-field fit [23].

B. Zeeman absorption spectroscopy

In order to achieve a definitive crystal-field analysis directional information is required. To achieve this, high resolution Zeeman absorption spectroscopy was performed for all three crystallographic axes, on the plethora of absorption lines observed through the infrared to the visible/near UV. Previous studies have determined the full g tensors of the $^4\text{I}_{15/2}\text{Z}_1$ and $^4\text{I}_{13/2}\text{Y}_1$ states for both sites through rotational Zeeman and electron paramagnetic resonance experiments [24, 25].

Figs. 2 and 3 show representative 4.2 K spectra of the $^4\text{I}_{15/2}\text{Z}_1 \rightarrow ^4\text{I}_{13/2}\text{Y}_1$ transition for site 1 and site 2 respectively under the influence of a magnetic field. The

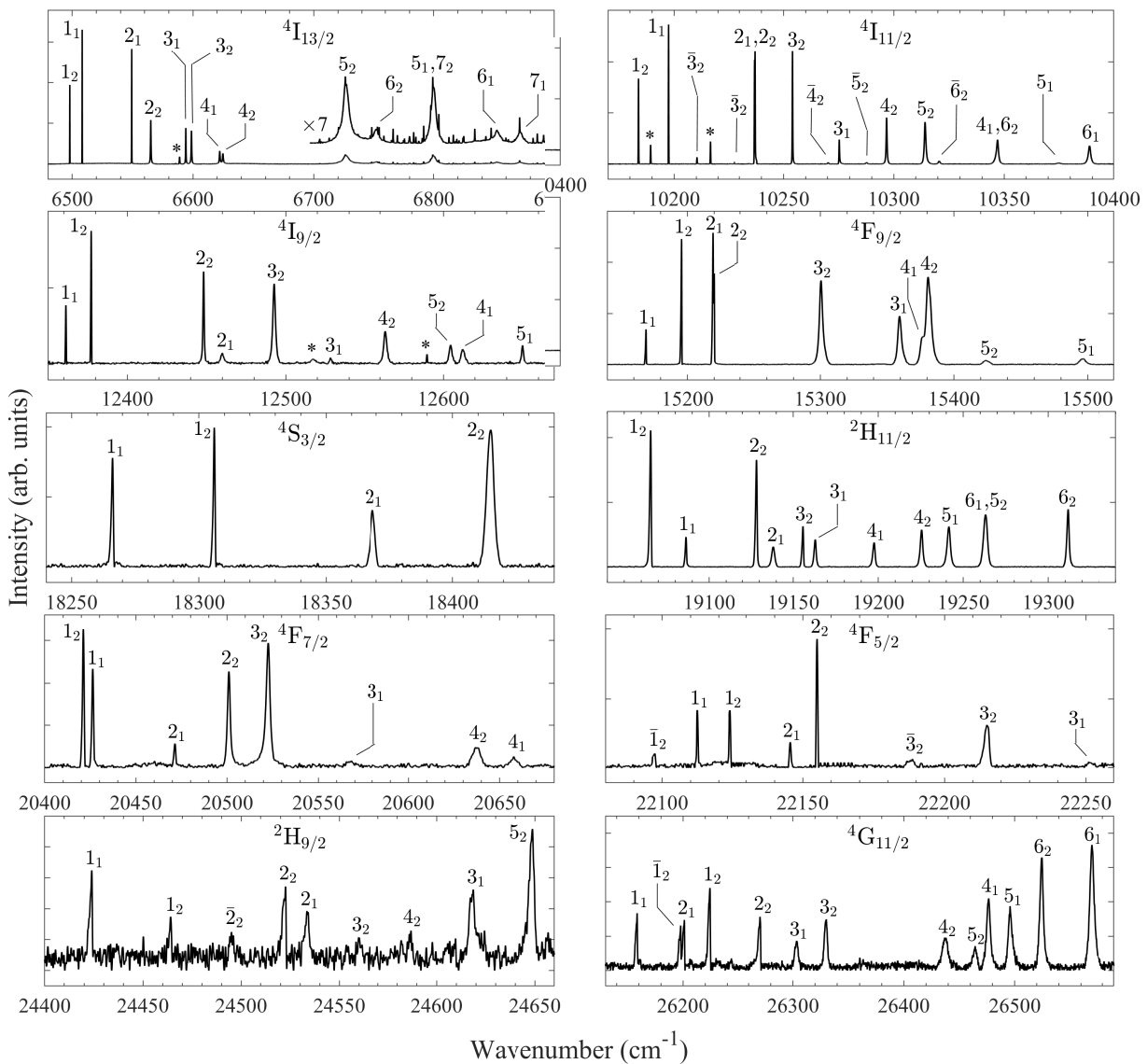


FIG. 1. 12 K absorption spectra of most excited multiplets up to the ${}^4G_{11/2}$ multiplet of $Y_2SiO_5:0.005\%Er^{3+}$. The transition labels indicate the ordering within the multiplet whilst a subscript gives the site assignment. Transitions from the Z_2 state are denoted with an overline. Spectral features labeled with an ‘*’ are unrelated to Er^{3+} . Transitions to the ${}^4F_{3/2}$ multiplet could not be observed.

top, middle and bottom panels show the Zeeman splittings for magnetic fields directed parallel to the D_1 , D_2 and b axes respectively. The left panels show Zeeman absorption spectra at magnetic field strengths represented by the vertical lines in the right panels. The right panels show the experimental and calculated splittings as a function of magnetic field, with the calculated zero field energies shifted as appropriate to overlay the splittings. It can be seen that the calculations are a good approximation to the experimental data. Asymmetries in the spectra result from the quadratic Zeeman effect, due to repulsion by nearby states.

A total of 68 g values (20 along the D_1 axis, 23 along the D_2 axis and 25 along the b axis) for site 1 and 70 g

values (25 along the D_1 axis, 24 along the D_2 axis and 21 along the b axis) for site 2 were able to be determined. These values are summarized in Tables I and II respectively. The g values could only be determined for states that have a splitting large enough to be resolved relative to the linewidth of the transition, within the linear splitting regime. For states above 22 000 cm^{-1} , most of the g values could not be determined due to insufficient signal and relatively broad spectral lines.

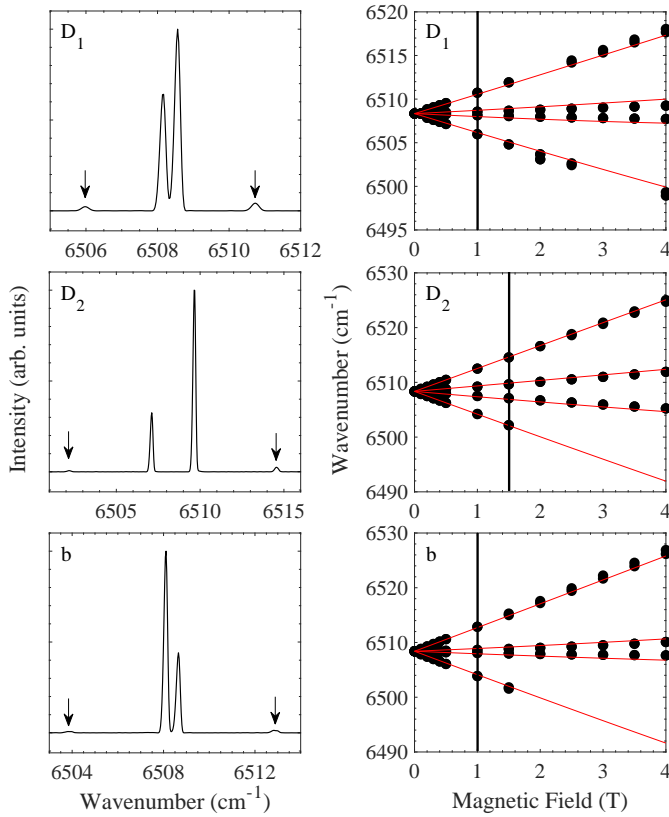


FIG. 2. Magnetic splittings of the site 1 $Z_1 \rightarrow Y_1$ transition for magnetic fields applied along the three crystallographic axes of Y_2SiO_5 . The top, middle and bottom panels shows $B \parallel D_1$, $B \parallel D_2$ and $B \parallel b$ respectively. The left panels show 4.2 K Zeeman absorption spectra at magnetic field strengths represented by the vertical lines in the right panels. The weak outer transitions are labeled with arrows to assist the reader. The right panels show the experimental splittings, represented by the circles, and the calculated splittings are represented by the red lines.

C. Parametrized crystal-field analysis

The Hamiltonian appropriate for modeling the $4f^{11}$ configuration of Er^{3+} is given in Equation (1). For more details the reader is directed to [29].

$$H = H_{FI} + H_{CF} + H_Z + H_{HF} + H_Q \quad (1)$$

The terms in the equation correspond to the free-ion, crystal-field, Zeeman, the nuclear magnetic dipole hyperfine, and the nuclear quadrupole hyperfine interactions respectively. The free-ion interaction includes effects such as the configuration barycenter, parameterized by E_{avg} , aspherical electrostatic repulsion, given by the Slater parameters, F_k , and the spin-orbit interaction, represented by ζ , in addition to two- and three-body relativistic interactions as well as higher order effects. Here we fixed the M^0 and P^2 parameters, and constrained the M^2 , M^4 , P^4 and P^6 parameters to the values and ratios defined by Ref. [37]. The crystal-field Hamiltonian used

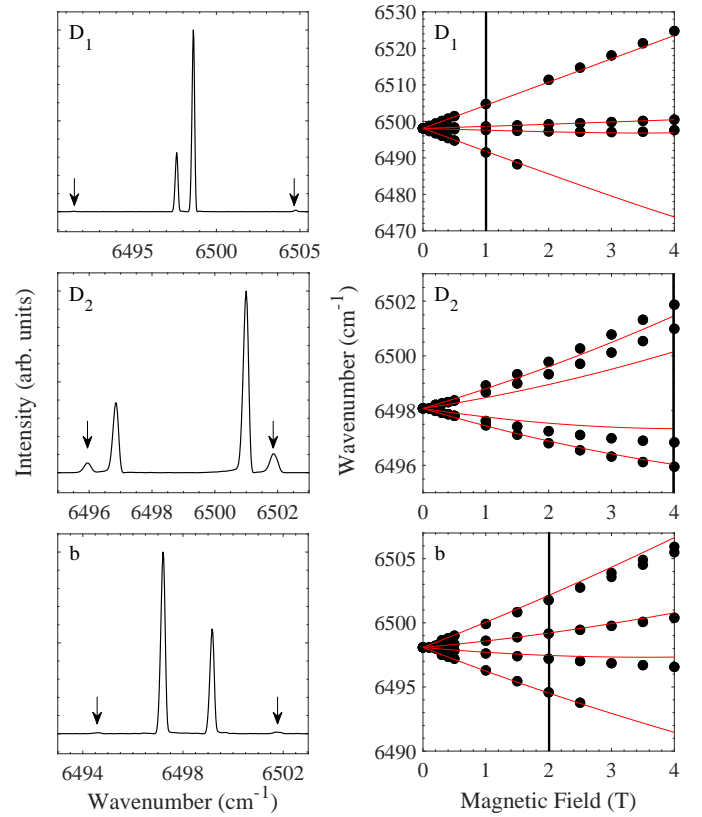


FIG. 3. Magnetic splittings of the site 2 $Z_1 \rightarrow Y_1$ transition for magnetic fields applied along the three crystallographic axes of Y_2SiO_5 . The top, middle and bottom panels shows $B \parallel D_1$, $B \parallel D_2$ and $B \parallel b$ respectively. The left panels show 4.2 K Zeeman absorption spectra at magnetic field strengths represented by the vertical lines in the right panels. The weak outer transitions are labeled with arrows to assist the reader. The right panels show the experimental splittings, represented by the circles, and the calculated splittings are represented by the red lines.

in this study has the form:

$$H_{CF} = \sum_{k,q} B_q^k C_q^{(k)} \quad (2)$$

Here $k = 2, 4, 6$ and $q = -k, \dots, k$. The B_q^k parameters are the crystal-field expansion coefficients and $C_q^{(k)}$ are spherical tensor operators using Wybourne's normalization [30]. All parameters with the exception of the axial ($q = 0$) parameters are complex, leading to a total of 27 independent values for the C_1 point group symmetry appropriate to Y_2SiO_5 . The Zeeman Hamiltonian has no free parameters while the magnetic dipole hyperfine, and the nuclear quadrupole interactions are represented by coupling constants a_l and a_Q respectively, which are required to be determined from experimental data [18]. In the fits reported here five free ion parameters, twenty seven crystal-field parameters and two hyperfine parameters were fitted to the experimental data.

To obtain a unique fit for such a low symmetry requires

orientational data. This is provided by measurements using magnetic fields in a variety of directions. The key magnetic-hyperfine data is reported using a spin Hamiltonian [31]:

$$\mathcal{H} = \mu_B \mathbf{B} \cdot \mathbf{g} \cdot \mathbf{S} + \mathbf{I} \cdot \mathbf{A} \cdot \mathbf{S} + \mathbf{I} \cdot \mathbf{Q} \cdot \mathbf{I} - \mu_n g_n \mathbf{B} \cdot \mathbf{I} \quad (3)$$

Here μ_B corresponds to the Bohr magneton, \mathbf{B} is the magnetic field vector, \mathbf{g} , \mathbf{A} and \mathbf{Q} are the magnetic g , hyperfine and electric-quadrupole tensors respectively. μ_n is the nuclear magneton while g_n is the nuclear g factor. \mathbf{S} and \mathbf{I} are vector representations of the electronic and nuclear spin operators respectively. Rather than fit to the tensors, in our fits we evaluate Hamiltonian (1) at various magnetic field directions [16]. This results in a separate Hamiltonian matrix for each set of data, evaluated at a particular magnetic field sampled from the parametric spiral:

$$\mathbf{B} = B_0 \begin{bmatrix} \sqrt{1-t^2} \cos(6\pi t) \\ \sqrt{1-t^2} \sin(6\pi t) \\ t \end{bmatrix}, \quad t \in [-1, 1] \quad (4)$$

Here B_0 is the magnitude of the magnetic field vector. As multiple Hamiltonian matrices must be diagonalized simultaneously, the hyperfine portion of the fit used an intermediate coupled effective Hamiltonian in a basis spanning only the $^4I_{15/2}$ and $^4I_{13/2}$ multiplets. This reduced the dimension of the hyperfine Hamiltonian from 2912 to 224 states, reducing the time required to perform the fit. The matrix elements of the crystal-field levels were truncated to 40 000 cm^{-1} to further increase performance. The starting parameters in the optimization routine were set to those found by Horvath *et al.* [16, 18]. A coarse fit was performed using a basin hopping algorithm, which attempts a random step followed by a local minimization [32, 33]. The Metropolis criterion was then applied to check if the random step is accepted and the algorithm was allowed to move to the newly found local minima [34]. The algorithm used for the local minimization was the bound optimization by quadratic approximation (BOBYQA) algorithm from the nonlinear-optimization (NLOpt) package [35]. Following this, a final fit was performed using simulated annealing. Simulated annealing has the advantage that the parameter uncertainties can be estimated using Markov chain Monte Carlo (MCMC) techniques through sampling the posterior probability distribution [36].

For site 1 a total of 350 experimental data points were fitted simultaneously and are as follows:

- 55 electronic energy levels up to the $^4G_{11/2}$ multiplet at $\sim 26\,500 \text{ cm}^{-1}$ including the $^4I_{15/2}Z_5 - Z_8$ states determined by Doualan *et al.* [23].
- 68 g values (20 along the D_1 axis, 23 along the D_2 axis and 25 along the b axis) corresponding to states up to the $^4F_{5/2}$ multiplet at $\sim 20\,500 \text{ cm}^{-1}$.

- 180 data points for the hyperfine splittings of the $^4I_{15/2}Z_1$ state, calculated from the \mathbf{g} , \mathbf{A} and \mathbf{Q} tensors determined by Chen *et al.* [25]. The energy of each hyperfine state except the ground state (which was set as zero) was sampled at equally spaced intervals according to Equation (4), with $B_0 = 0.05 \text{ T}$.
- 12 data points for the magnetic splittings of the $^4I_{13/2}Y_1$ state, calculated from the \mathbf{g} tensor determined by Sun *et al.* [24], also sampled at equally spaced intervals according to Equation (4), with $B_0 = 0.05 \text{ T}$.
- 4 data points from low-frequency Raman heterodyne measurements, calculated from a three dimensional curvature tensor of transition energy with respect to a magnetic field, obtained from [16]. The four data points were sampled at magnetic fields of $[0\ 0\ 0]$, $[0.5\ 0\ 0]$, $[0\ 0.5\ 0]$, $[0\ 0\ 0.5]$ (with axes $[D_1\ D_2\ b]$ and units of mT).
- 31 data points of high frequency Raman heterodyne spectroscopy along the D_2 direction as determined in [16]. Second order polynomials were fitted and sampled at magnetic field strengths of 0.0, 0.3 and 0.5 mT. Nine transitions were fitted using this method whereas four of the transitions have a very steep gradient around zero field and therefore were only sampled at 0.5 mT.

To date there has been no Raman heterodyne studies performed on site 2 of $\text{Er}^{3+}:\text{Y}_2\text{SiO}_5$ and therefore 319 experimental data points were fitted simultaneously and are as follows:

- 57 electronic energy levels up to the $^4G_{11/2}$ multiplet at $\sim 26\,500 \text{ cm}^{-1}$ including the $^4I_{15/2}Z_5 - Z_8$ states determined by Doualan *et al.* [23].
- 70 g values (25 along the D_1 axis, 24 along the D_2 axis and 21 along the b axis) corresponding to states up to the $^4F_{5/2}$ multiplet at $\sim 20\,500 \text{ cm}^{-1}$.
- 180 data points for the hyperfine splittings of the $^4I_{15/2}Z_1$ state, calculated from the \mathbf{g} , \mathbf{A} and \mathbf{Q} tensors determined by Chen *et al.* [25]. The energy of each hyperfine state except the ground state (which was set as zero) was sampled at equally spaced intervals according to Equation (4), with $B_0 = 0.05 \text{ T}$.
- 12 data points for the magnetic splittings of the $^4I_{13/2}Y_1$ state, calculated from the \mathbf{g} tensor determined by Sun *et al.* [24], also sampled at equally spaced intervals according to Equation (4), with $B_0 = 0.05 \text{ T}$.

Table III shows the fitted free-ion, crystal field, and hyperfine parameters for both sites in $\text{Er}^{3+}:\text{Y}_2\text{SiO}_5$. The values obtained by Horvath *et al.* [16, 18] are provided

TABLE I. Calculated and experimental electronic energies levels and g values up to 27 000 cm^{-1} for site 1 in $\text{Er}^{3+}:\text{Y}_2\text{SiO}_5$. All energies are in cm^{-1} . Levels marked with a ‘-’ were not assigned. Levels marked with an ‘*’ are assignments made by Doualan *et al.* [23].

Multiplet	State	Energies			g values					
		Calc.	Exp.	Difference	D_1 axis		D_2 axis		b axis	
					Calc.	Exp.	Calc.	Exp.	Calc.	Exp.
$^4\text{I}_{15/2}$	Z ₁	-10	0	10	5.47	5.46	11.06	10.91	8.18	8.36
	Z ₂	39	39	0	6.67	-	1.50	-	8.19	-
	Z ₃	72	84	12	3.98	-	7.07	-	2.35	-
	Z ₄	111	102	-9	3.93	-	9.34	-	4.23	-
	Z ₅	179	172*	-7	4.08	-	8.58	-	7.35	-
	Z ₆	416	424*	8	10.22	-	7.62	-	3.68	-
	Z ₇	474	481*	7	10.79	-	7.14	-	4.42	-
	Z ₈	509	513*	4	8.30	-	12.08	-	6.50	-
$^4\text{I}_{13/2}$	Y ₁	6518	6508	-10	3.93	4.64	6.82	6.90	10.24	10.00
	Y ₂	6564	6549	-15	5.93	4.24	4.35	4.41	5.69	7.77
	Y ₃	6599	6598	-1	6.59	4.54	4.73	3.04	2.56	6.10
	Y ₄	6637	6624	-13	3.43	9.32	6.29	5.44	5.97	1.87
	Y ₅	6805	6800	-5	8.47	-	6.16	-	2.43	-
	Y ₆	6866	6852	-14	9.13	-	5.57	-	4.56	-
	Y ₇	6887	6871	-16	7.32	-	9.66	-	5.23	-
$^4\text{I}_{11/2}$	A ₁	10189	10197	8	3.30	3.89	3.67	4.80	8.75	8.23
	A ₂	10231	10237	6	4.43	3.31	3.15	-	4.04	5.99
	A ₃	10258	10275	17	4.76	5.41	2.84	4.00	4.27	3.30
	A ₄	10345	10347	2	6.58	3.51	4.44	-	1.82	-
	A ₅	10386	10375	-11	6.87	5.33	4.13	5.31	3.73	-
	A ₆	10396	10389	-7	5.65	7.28	7.11	6.21	3.79	1.66
$^4\text{I}_{9/2}$	B ₁	12337	12362	25	4.39	3.75	3.16	3.68	1.64	1.87
	B ₂	12430	12461	31	1.99	-	1.40	2.10	5.51	4.03
	B ₃	12532	12529	-3	1.61	-	3.08	2.01	3.27	3.73
	B ₄	12606	12613	7	2.60	-	3.47	-	1.55	1.65
	B ₅	12656	12651	-5	3.31	3.66	3.27	1.98	2.26	2.44
$^4\text{F}_{9/2}$	D ₁	15185	15170	-15	8.60	7.86	0.68	1.76	3.42	4.61
	D ₂	15236	15220	-16	2.68	1.39	7.51	6.84	2.05	3.21
	D ₃	15360	15360	0	2.54	0.54	2.66	-	2.72	2.30
	D ₄	15402	15377	-25	2.41	-	4.90	-	2.67	-
	D ₅	15493	15497	4	4.04	-	3.64	-	5.88	-
$^4\text{S}_{3/2}$	E ₁	18272	18267	-5	4.13	3.64	2.03	3.00	2.84	2.77
	E ₂	18359	18369	10	2.43	-	2.44	2.24	4.37	-
$^2\text{H}_{11/2}$	F ₁	19115	19087	-28	2.66	8.47	9.21	7.93	4.89	0.89
	F ₂	19152	19139	-13	5.97	-	6.51	-	2.62	-
	F ₃	19177	19164	-13	4.12	-	5.45	2.08	7.23	10.36
	F ₄	19242	19242	0	0.38	-	2.60	4.72	3.67	3.79
	F ₅	19277	19264	-13	3.88	-	7.64	-	0.68	-
	F ₆	19302	19312	10	4.64	4.93	3.52	4.80	5.15	5.20
$^4\text{F}_{7/2}$	G ₁	20424	20430	6	4.77	5.91	3.99	3.92	3.16	3.25
	G ₂	20468	20475	7	2.91	-	3.84	4.58	3.16	1.90
	G ₃	20557	20570	13	3.79	-	2.79	-	2.56	-
	G ₄	20633	20660	27	3.00	-	2.43	-	6.97	-
$^4\text{F}_{5/2}$	H ₁	22099	22115	16	1.29	-	1.64	-	2.08	1.18
	H ₂	22130	22148	18	3.40	-	1.96	-	1.51	-
	H ₃	22217	22255	38	1.18	-	2.76	-	2.54	-
$^4\text{F}_{3/2}$	I ₁	22470	-	-	1.90	-	1.08	-	0.72	-
	I ₂	22601	-	-	0.80	-	0.85	-	1.36	-
$^2\text{H}_{9/2}$	K ₁	24403	24423	20	5.70	-	3.49	-	2.49	-
	K ₂	24515	24534	19	2.18	-	1.79	-	5.53	-
	K ₃	24594	24618	24	2.08	-	2.41	-	4.51	-
	K ₄	24639	-	-	2.18	-	3.77	-	3.69	-
	K ₅	24686	-	-	3.88	-	3.78	-	2.66	-
$^4\text{G}_{11/2}$	L ₁	26207	26159	-48	4.51	-	8.68	-	5.03	-
	L ₂	26223	26202	-21	6.93	-	5.44	-	4.47	-
	L ₃	26322	26304	-18	4.74	-	3.95	-	2.72	-
	L ₄	26469	26477	8	1.88	-	3.85	-	4.04	-
	L ₅	26514	26497	-17	4.58	-	6.93	-	1.13	-
	L ₆	26577	26571	-6	3.82	-	5.95	-	3.43	-

TABLE II. Calculated and experimental electronic energies levels and g values up to 27 000 cm^{-1} for site 2 in $\text{Er}^{3+}:\text{Y}_2\text{SiO}_5$. All energies are in cm^{-1} . Levels marked with a ‘-’ were not assigned. Levels marked with an ‘*’ are assignments made by Doualan *et al.* [23].

Multiplet	State	Energies			g values					
		Calc.	Exp.	Difference	D_1 axis		D_2 axis		b axis	
					Calc.	Exp.	Calc.	Exp.	Calc.	Exp.
$^4\text{I}_{15/2}$	Z ₁	-1	0	1	14.65	15.31	2.21	2.66	3.13	2.84
	Z ₂	29	27	-2	8.58	-	5.27	-	4.93	-
	Z ₃	66	62	-4	3.07	-	6.40	-	6.95	-
	Z ₄	129	126	-3	5.21	-	11.48	-	4.50	-
	Z ₅	170	169*	-1	6.52	-	4.03	-	6.98	-
	Z ₆	313	314*	1	3.71	-	7.17	-	7.18	-
	Z ₇	347	350*	3	6.57	-	11.73	-	3.72	-
	Z ₈	408	415*	7	5.18	-	4.11	-	13.96	-
$^4\text{I}_{13/2}$	Y ₁	6515	6498	-17	12.37	13.14	0.70	0.46	5.01	4.93
	Y ₂	6570	6565	-5	7.82	8.23	3.61	2.16	2.46	5.45
	Y ₃	6596	6594	-2	3.36	2.61	9.33	10.75	4.04	2.63
	Y ₄	6637	6622	-15	5.73	6.04	3.35	4.75	5.72	4.36
	Y ₅	6733	6726	-7	3.15	-	4.85	-	7.24	-
	Y ₆	6767	6752	-15	6.11	-	10.58	10.88	3.04	-
	Y ₇	6813	6800	-13	3.88	-	3.60	-	11.37	-
$^4\text{I}_{11/2}$	A ₁	10176	10184	8	9.60	10.04	0.30	-	4.07	-
	A ₂	10223	10237	14	5.82	6.71	3.80	5.19	2.81	3.92
	A ₃	10243	10254	11	3.36	3.06	2.66	5.44	5.02	-
	A ₄	10296	10297	1	2.80	3.91	3.78	3.05	4.71	3.71
	A ₅	10317	10314	-3	4.34	5.53	8.12	5.95	1.49	-
	A ₆	10347	10347	0	2.74	1.14	2.88	4.42	8.95	9.35
$^4\text{I}_{9/2}$	B ₁	12357	12378	21	0.62	1.17	4.17	3.08	3.00	4.02
	B ₂	12424	12449	25	4.23	3.23	2.24	2.05	2.87	1.05
	B ₃	12471	12494	23	1.85	3.54	2.52	-	2.61	-
	B ₄	12542	12564	22	2.18	2.00	3.67	3.63	2.54	3.53
	B ₅	12599	12605	6	2.27	-	1.76	-	4.39	-
$^4\text{F}_{9/2}$	D ₁	15211	15196	-15	2.79	3.72	6.26	5.83	3.89	5.02
	D ₂	15234	15221	-13	2.90	2.40	3.00	-	3.35	5.20
	D ₃	15309	15302	-7	3.90	4.41	3.03	4.11	4.44	3.73
	D ₄	15390	15382	-8	6.66	-	1.99	-	2.68	-
	D ₅	15437	15425	-12	7.66	-	3.76	-	2.17	-
$^4\text{S}_{3/2}$	E ₁	18307	18306	-1	1.91	1.83	2.66	2.99	4.14	7.22
	E ₂	18405	18415	10	4.77	-	1.30	-	1.91	-
$^2\text{H}_{11/2}$	F ₁	19093	19067	-26	6.29	7.39	8.74	8.77	3.89	3.42
	F ₂	19143	19129	-14	7.92	8.47	2.68	4.57	3.91	2.75
	F ₃	19166	19157	-9	0.76	2.36	5.58	4.72	8.98	8.04
	F ₄	19203	19199	-4	2.24	2.16	4.47	3.97	3.89	4.41
	F ₅	19242	19226	-16	3.65	-	7.81	8.00	3.04	-
	F ₆	19255	19264	9	5.70	-	3.82	-	4.86	-
$^4\text{F}_{7/2}$	G ₁	20421	20424	3	2.19	2.74	3.08	3.57	6.85	6.47
	G ₂	20489	20504	15	1.44	-	3.16	5.01	3.61	-
	G ₃	20519	20526	7	4.55	-	3.22	-	2.11	-
	G ₄	20623	20640	17	7.30	-	0.95	-	2.90	-
$^4\text{F}_{5/2}$	H ₁	22109	22126	17	0.76	0.62	1.55	-	3.79	-
	H ₂	22146	22157	11	2.39	-	3.24	-	1.85	1.35
	H ₃	22196	22218	22	3.98	-	0.89	-	1.31	-
$^4\text{F}_{3/2}$	I ₁	22454	-	-	0.74	-	1.36	-	1.59	-
	I ₂	22584	-	-	1.54	-	0.22	-	0.71	-
$^2\text{H}_{9/2}$	K ₁	24442	24464	22	1.40	-	5.75	-	3.23	-
	K ₂	24513	24522	9	3.28	-	3.05	-	3.11	-
	K ₃	24556	24557	1	3.42	-	2.73	-	3.28	-
	K ₄	24605	24587	-18	1.99	-	4.23	-	3.14	-
	K ₅	24657	24649	-8	3.22	-	3.62	-	3.87	-
$^4\text{G}_{11/2}$	L ₁	26251	26225	-26	6.43	-	9.77	-	3.78	-
	L ₂	26278	26271	-7	5.74	-	2.34	-	8.61	-
	L ₃	26335	26331	-4	3.36	-	2.77	-	5.10	-
	L ₄	26435	26438	3	3.29	-	4.59	-	3.57	-
	L ₅	26485	26465	-20	3.46	-	8.73	-	2.76	-
	L ₆	26519	26525	6	6.70	-	4.91	-	2.70	-

TABLE III. Fitted values for the free-ion, crystal-field and hyperfine parameters and their related uncertainties of site 1 and site 2 in $\text{Er}^{3+}:\text{Y}_2\text{SiO}_5$. All values are in cm^{-1} . Parameters determined by Horvath *et al.* are also included for comparison [16, 18].

Parameter	Site 1			Site 2			
	This study	Uncertainty	Ref. [16]	Ref. [18]	This study	Uncertainty	Ref. [18]
E_{avg}	35491.3	0.1	35503.5	–	35507.5	0.1	–
F^2	95805.7	1.0	96029.6	95346	96121.9	1.3	95721
F^4	67869.7	3.4	67670.6	68525	67722.4	4.5	68564
F^6	53148.2	2.5	53167.1	52804	53241.2	3.1	52999
ζ	2360.5	0.1	2362.9	2358	2362.3	0.1	2356
B_0^2	-479.6	6.1	-149.8	-563	389.0	3.7	354
B_1^2	471.4+143.8i	2.9 + 3.0i	420.6+396.0i	558+280i	-325.7-95.8i	2.7 + 3.0i	498.6807+274i
B_2^2	125.5-2.0i	2.8 + 2.3i	-228.5+27.6i	143-121i	-368.5+53.7i	1.8 + 2.0i	-75.8028+60i
B_0^4	-640.6	31.3	1131.2	-125	17.2	15.5	226
B_1^4	288.8+924.1i	7.2 + 25.3i	985.7+34.2i	225-831i	-378.7-519.5i	5.1 + 9.3i	-657.8381+593i
B_2^4	-273.9+320.9i	11.1 + 16.7i	296.8+145.0i	-48-945i	-72.0-146.0i	5.7 + 6.7i	335.7827+253i
B_3^4	-873.7-367.8i	20.7 + 9.7i	-402.3-381.7i	-615-688i	-890.8+570.4i	9.5 + 7.3i	-71.3262-46i
B_4^4	-600.8+1210.5i	23.7 + 9.2i	-282.3+1114.3i	744-102i	-198.7-567.9i	7.8 + 5.2i	-813.9654+64i
B_0^6	145.7	13.2	-263.2	-28	73.4	4.3	219
B_1^6	-105.9-329.0i	2.9 + 4.0i	111.9+222.9i	49+199i	-37.5+49.9i	3.4 + 5.7i	-127+197i
B_2^6	-119.9+164.1i	7.7 + 8.8i	124.7+195.9i	120-107i	135.5+60.6i	4.5 + 1.5i	-36-47i
B_3^6	1.1+133.3i	6.7 + 4.5i	-97.9+139.7i	195-55i	-166.7+131.8i	2.6 + 4.0i	17-108i
B_4^6	-84.6+36.9i	5.0 + 4.5i	-93.7-145.0i	-287-161i	227.2+47.6i	1.2 + 3.0i	-100+77i
B_5^6	75.5+6.9i	4.3 + 6.6i	13.9+109.5i	-117+162i	119.5+64.3i	3.7 + 3.2i	-263+103i
B_6^6	-48.5+118.0i	6.2 + 4.2i	3.0-108.6i	136+186i	37.6-41.3i	3.5 + 2.8i	12-26i
S^2	386.6	–	399.0	483.0	363.1	–	397.9
S^4	948.2	–	862.9	824.6	653.3	–	607.5
S^6	183.8	–	189.6	218.6	151.5	–	171.4
a_l	0.005306	0.000008	0.005466	0.0059	0.005389	0.000012	0.0069
a_Q	0.0554	0.0020	0.0716	0.0800	0.0240	0.0024	0.0808

TABLE IV. Parameters that were held fixed during the fitting process and were set to those found by Carnall *et al.* in $\text{Er}^{3+}:\text{LaF}_3$ [37].

Parameter	Value (cm^{-1})
α	17.79
β	-582.10
γ	1800.00
T^2	400.00
T^3	43.00
T^4	73.00
T^6	-271.00
T^7	308.00
T^8	299.00
M^0	3.86
P^2	594.00

for comparison. The two- and three-body interactions and higher order effects in the free-ion Hamiltonian were held fixed to the values obtained by Carnall *et al.* in $\text{Er}^{3+}:\text{LaF}_3$ and are given in Table IV [37]. The uncertainties of the fitted parameters were estimated through the use of the MCMC techniques in order to sample the posterior probability distribution [36]. A total of 3 million trials were undertaken for both sites with 343 158

accepted steps for site 1 and 278 705 accepted steps for site 2. This aligns with the Metropolis algorithms $\sim 10\%$ acceptance rate recommended for this technique which was fine tuned through altering the step size in the optimization routine [36]. The algorithm was allowed to ‘burn in’ and every 10^{th} element of the last 30 000 steps was selected to ensure that the samples were not correlated.

The calculated energy levels and g values up to the $^4\text{G}_{11/2}$ multiplet of $\text{Er}^{3+}:\text{Y}_2\text{SiO}_5$ for site 1 and site 2 are given in Tables I and II respectively, along with the corresponding experimental values. The overall agreement is very good, having standard deviations comparable to the previous work [16, 18], but for considerably more data, distributed over a larger portion of the $4f^{11}$ configuration.

Spin Hamiltonian parameters derived from the crystal-field model for the $^4\text{I}_{15/2}\text{Z}_1$ and $^4\text{I}_{13/2}\text{Y}_1$ states relevant to the $1.5\ \mu\text{m}$ telecommunications transition are presented in Table V. Those calculated by Horvath *et al.* [16], and the experimentally determined values of Chen *et al.* and Sun *et al.* [24, 25], are also included for comparison. The close agreement between our calculated parameters and those derived from measurements indicate that the hyperfine structure of the $^4\text{I}_{15/2}\text{Z}_1$ and $^4\text{I}_{13/2}\text{Y}_1$ states are well accounted for by our fit.

Magnetic-splitting data is crucial to fitting the crystal-

TABLE V. Spin Hamiltonian parameters for the ${}^4I_{15/2}Z_1$ and ${}^4I_{13/2}Y_1$ states for site 1 and site 2 in $\text{Er}^{3+}:\text{Y}_2\text{SiO}_5$. All A and Q values are in MHz.

State	Study	Site 1						Site 2					
		g_{xx}	g_{yy}	g_{zz}	g_{xy}	g_{xz}	g_{yz}	g_{xx}	g_{yy}	g_{zz}	g_{xy}	g_{xz}	g_{yz}
${}^4I_{15/2}Z_1$	This study	3.03	8.75	4.92	-3.00	-3.44	5.74	14.47	1.51	1.65	-1.89	2.37	0.02
	Ref. [16]	2.10	8.37	5.49	-3.43	-3.21	5.16	-	-	-	-	-	-
	Ref. [25]	2.90	8.90	5.12	-2.95	-3.56	5.57	14.37	1.93	1.44	-1.77	2.40	-0.43
	Ref. [24]	3.07	8.16	5.79	-3.14	-3.40	5.76	14.65	1.97	0.90	-2.12	2.55	-0.55
${}^4I_{13/2}Y_1$	This study	1.63	3.66	8.29	-1.86	-2.98	5.11	11.58	0.31	2.13	-0.69	4.44	-0.26
	Ref. [16]	2.04	4.44	7.94	-2.24	-3.40	5.15	-	-	-	-	-	-
	Ref. [24]	1.95	4.23	7.89	-2.21	-3.58	4.99	12.03	0.21	1.77	-5.85	4.52	-0.30
		A_{xx}	A_{yy}	A_{zz}	A_{xy}	A_{xz}	A_{yz}	A_{xx}	A_{yy}	A_{zz}	A_{xy}	A_{xz}	A_{yz}
${}^4I_{15/2}Z_1$	This study	317.20	917.44	515.83	-314.96	-361.63	602.05	1541.77	159.17	175.52	-200.91	253.34	1.61
	Ref. [16]	200.80	911.27	586.95	-344.23	-362.61	586.95	-	-	-	-	-	-
	Ref. [25]	274.29	827.50	706.15	-202.52	-350.82	635.15	-1565.3	-15.3	127.8	219.0	-124.4	-0.7
${}^4I_{13/2}Y_1$	This study	206.60	466.60	1061.93	-236.41	-380.64	653.32	1504.47	40.73	276.53	-90.45	577.51	-34.26
	Ref. [16]	271.96	583.12	1058.43	-293.37	-447.76	684.97	-	-	-	-	-	-
		Q_{xx}	Q_{yy}	Q_{zz}	Q_{xy}	Q_{xz}	Q_{yz}	Q_{xx}	Q_{yy}	Q_{zz}	Q_{xy}	Q_{xz}	Q_{yz}
${}^4I_{15/2}Z_1$	This study	4.89	-4.23	-0.67	3.95	4.23	-5.39	-4.49	2.81	1.69	0.85	-1.45	-1.15
	Ref. [16]	9.32	-6.37	-2.95	1.92	2.26	-9.55	-	-	-	-	-	-
	Ref. [25]	10.40	-5.95	-4.44	-9.12	-9.96	-14.32	-10.5	-19.5	30.0	-22.8	-3.1	-17.7
${}^4I_{13/2}Y_1$	This study	5.90	0.42	-6.32	2.30	4.44	-5.31	-4.16	3.03	1.13	0.44	-2.73	-0.42
	Ref. [16]	6.84	0.30	-7.13	3.62	5.54	-7.13	-	-	-	-	-	-

TABLE VI. Calculated and experimental ${}^4I_{15/2}Z_1$ ground and ${}^4I_{13/2}Y_1$ excited state hyperfine splittings for site 2 with a magnetic field of 7 T applied along the D_1 axis [5]. The calculated splittings were determined from our crystal-field model. All values are in MHz.

Splittings	${}^4I_{15/2}Z_1$		${}^4I_{13/2}Y_1$	
	This study	Ref. [5]	This study	Ref. [5]
$\Delta(1, 2)$	897	995	928	994
$\Delta(2, 3)$	881	943	912	972
$\Delta(3, 4)$	865	898	895	953
$\Delta(4, 5)$	849	862	879	935
$\Delta(5, 6)$	833	831	863	918
$\Delta(6, 7)$	817	810	847	903
$\Delta(7, 8)$	801	796	831	889

field parameters in C_1 symmetry. In the absence of magnetic data, an arbitrary rotation about *any* axis leaves the electronic energy levels invariant. Note, however, that there are two magnetically-inequivalent sites, related by a C_2 rotation about the b axis of the crystal (our z axis). We list only one set, since the parameter sets for the other orientation may be obtained by multiplying all of the crystal-field parameters with odd q by -1 .

A measure of the magnitude of the crystal-field is given by crystal-field strength parameters defined as [39]:

$$S^k = \left[\frac{1}{2k+1} \left((B_0^k)^2 + 2 \sum_{q>0} |B_q^k|^2 \right) \right]^{1/2} \quad (5)$$

These parameters are listed in Table III. As expected, the crystal-field strength parameters for site 1, identified as

the 6-coordinate site, are higher than for the 7-coordinate site 2, particularly the S^4 parameter.

The crystal-field parameters determined in this study differ from previous work by Horvath *et al.* [16, 18]. This is to be expected, as we have added a significant quantity of new data, in the form of electronic energy levels and g values. In previous work, magnetic data were confined to the ${}^4I_{15/2}Z_1$ and ${}^4I_{13/2}Y_1$ states.

We have demonstrated excellent fits to experimental data from both sites over a wide range of energies. We now address the *predictive* ability of the model. We begin by discussing the optical polarization behavior of the ${}^4I_{15/2}Z_1 \rightarrow {}^4I_{13/2}Y_1$ transition. We will then discuss high-field Zeeman-hyperfine experiments.

The precise orientation of transition dipole moments is significant for some applications [9]. We do not yet have a model for electric-dipole moments for rare-earth ions in this crystal, but we can calculate the magnetic dipole moments from the wave functions. Petit *et al.* [38] have recently made novel measurements that separate the variation of magnetic-dipole moments from the variation of electric-dipole moments of the ${}^4I_{15/2}Z_1 \rightarrow {}^4I_{13/2}Y_1$ transition for both sites by rotating a cylindrical crystal about the b crystal axis.

In Fig. 4. we show the experimental and calculated angular variations of the absorption depth of the ${}^4I_{15/2}Z_1 \rightarrow {}^4I_{13/2}Y_1$ transition as the crystal is rotated about the b axis. The electric vector of the light was aligned with the b axis and the propagation vector, \vec{k} , was rotated in the D_1, D_2 plane (with $\theta = 0$ corresponding to $\vec{k} \parallel D_1$, and $\theta = 90^\circ$ corresponding to $\vec{k} \parallel D_2$). In this orientation, the magnetic vector is also in the D_1, D_2

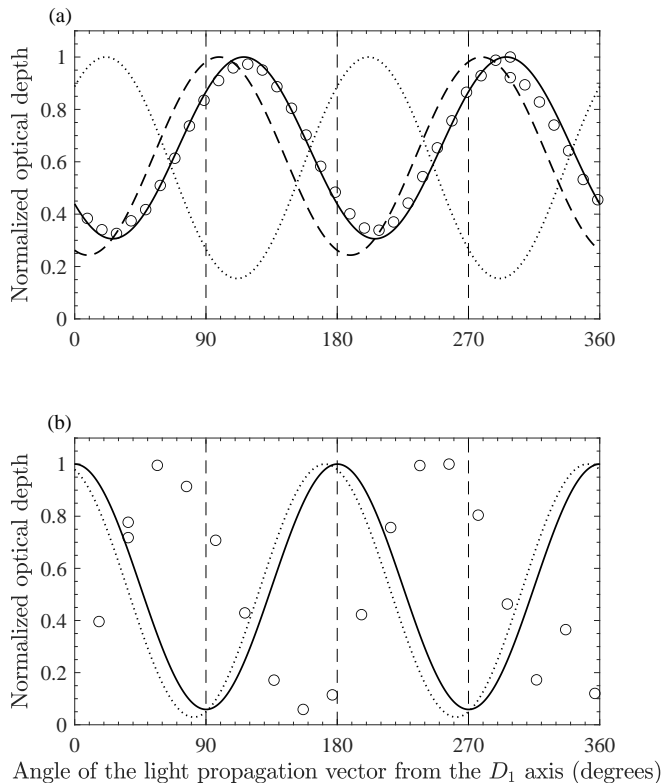


FIG. 4. Polarization behavior of the ${}^4I_{15/2}Z_1 \rightarrow {}^4I_{13/2}Y_1$ transition for (a) site 1 and (b) site 2. The open circles represent the experimentally determined values [38]. The solid line is the prediction from this study, the dotted line is the prediction using the crystal-field parameters from [18] whilst the dashed line is the prediction using the crystal-field parameters from [16].

plane. The electric dipole contribution to the absorption depth is constant as the crystal is rotated.

Our prediction is shown as the solid line in Fig. 4. We predict the maximum optical depth to be at 295.9° for site 1, while the experimental maximum is at 298.6° . For site 2, we predict the maximum optical depth to be at 180.1° , while the experimental maximum is at 256.6° [38]. Thus, the calculation is roughly out of phase with the experimental measurement for site 2.

Figure 4 also shows predictions using crystal-field parameters from Horvath *et al.* [16, 18]. For site 1, the parameters from Ref. [16] gives predictions nearly in phase with the measurements, while the parameters from Ref. [18] gave predictions that are out of phase with the measurements. The fit in Ref. [18] did not include data for

the hyperfine splitting of the excited state, ${}^4I_{13/2}Y_1$. Excited state hyperfine data for site 1 is included in Ref. [16] and our current fit, and this may explain the differences. For site 2, neither Ref. [18], nor the current fit include hyperfine data for the excited state, and it is possible that the addition of such data might bring the calculations into agreement with the measurements.

We now discuss high-field Zeeman measurements. For an isolated Kramers doublet, a spin-Hamiltonian approach breaks down at high magnetic fields, when mixing of electronic states by the Zeeman interaction becomes significant. This non-linearity is apparent even at 4 T in the data presented in Fig. 3. Rančić *et al.* [5] have measured hyperfine splittings for the ${}^4I_{15/2}Z_1$ and excited ${}^4I_{13/2}Y_1$ states at a magnetic field of 7 T applied along the D_1 axis for site 2. Table VI compares predictions from our crystal-field model with the experimental splittings. The predictions agree with the experimentally determined values to within 10 %. The site 2 fit does not contain any data for the hyperfine splitting of the excited state, and with more data in the fit, better agreement could be expected.

IV. CONCLUSIONS

We have reported a parametrized crystal-field analysis for both C_1 symmetry sites in Er^{3+} doped Y_2SiO_5 which uses crystal-field energy levels up to $27\,000\text{ cm}^{-1}$, approximately 70 electronic g-values per site and electron-nuclear interactions within crystal-field levels of the two lowest energy multiplets as data inputs. The crucial feature of the analysis performed here is that the data input includes directional information (i.e. g values) which spans a considerable portion of the entire $4f^{11}$ configuration; this is required to obtain well determined crystal-field parameters in sites of such low point group symmetry. We demonstrate that the analysis presented here can *predict* the high-field Zeeman-hyperfine splittings (splittings measured in the non-linear regime [5]) as well as optical polarization behavior for the telecommunications transitions near $1.5\ \mu\text{m}$ [38].

ACKNOWLEDGMENTS

N.L.J. would like to thank the Dodd-Walls Centre for Photonic and Quantum Technologies for the provision of a PhD studentship. The technical assistance of Mr. S. Hemmingson, Mr. R. J. Thirkettle and Mr. G. MacDonald is gratefully acknowledged.

[1] M. A. Nielsen, *Quantum Computation and Quantum Information* (Cambridge University Press, 2010).

[2] T. Zhong, J. M. Kindem, J. G. Bartholomew, J. Rochman, I. Craiciu, E. Miyazono, M. Bettinelli,

- E. Cavalli, V. Verma, S. W. Nam, F. Marsili, M. D. Shaw, A. D. Beyer, and A. Faraon, Nanophotonic rare-earth quantum memory with optically controlled retrieval, *Science* **357**, 1392 (2017).
- [3] H. de Riedmatten, M. Afzelius, M. U. Staudt, C. Simon, and N. Gisin, A solid-state light-matter interface at the single-photon level, *Nature* **456**, 773 (2008).
- [4] M. Zhong, M. P. Hedges, R. L. Ahlefeldt, J. G. Bartholomew, S. E. Beavan, S. M. Wittig, J. J. Longdell, and M. J. Sellars, Optically addressable nuclear spins in a solid with a six-hour coherence time, *Nature* **517**, 177 (2015).
- [5] M. Rančić, M. P. Hedges, R. L. Ahlefeldt, and M. J. Sellars, Coherence time of over a second in a telecom-compatible quantum memory storage material, *Nat. Phys* **14**, 50–54 (2018).
- [6] J. J. Longdell and M. J. Sellars, Experimental demonstration of quantum-state tomography and qubit-qubit interactions for rare-earth-metal-ion-based solid-state qubits, *Phys. Rev. A* **69**, 032307 (2004).
- [7] L. Rippe, B. Julsgaard, A. Walther, Y. Ying, and S. Kröll, Experimental quantum-state tomography of a solid-state qubit, *Phys. Rev. A* **77**, 022307 (2008).
- [8] A. M. Dibos, M. Raha, C. M. Phenicie, and J. D. Thompson, Atomic source of single photons in the telecom band, *Phys. Rev. Lett.* **120**, 243601 (2018).
- [9] S. Chen, M. Raha, C. M. Phenicie, S. Ourari, and J. D. Thompson, Parallel single-shot measurement and coherent control of solid-state spins below the diffraction limit, *Science* **370**, 592 (2020).
- [10] J. Wesenberg and K. Mølmer, Robust quantum gates and a bus architecture for quantum computing with rare-earth-ion-doped crystals, *Phys. Rev. A* **68**, 012320 (2003).
- [11] E. Fraval, M. J. Sellars, A. Morrison, and A. Ferris, Pr–Y interaction in $\text{Pr}^{3+}:\text{Y}_2\text{SiO}_5$, *J. Lumin.* **107**, 347 (2004).
- [12] B. G. Wybourne and L. Smentek, *Optical Spectroscopy of Lanthanides: Magnetic and Hyperfine Interactions*, 1st ed. (CRC Press, 2007).
- [13] G. Heinze, C. Hubrich, and T. Halfmann, Stopped light and image storage by electromagnetically induced transparency up to the regime of one minute, *Phys. Rev. Lett.* **111**, 033601 (2013).
- [14] J. J. Longdell, M. J. Sellars, and N. B. Manson, Hyperfine interaction in ground and excited states of praseodymium-doped yttrium orthosilicate, *Phys. Rev. B* **66**, 035101 (2002).
- [15] Y. Sun, C. W. Thiel, R. L. Cone, R. W. Equall, and R. L. Hutchison, Recent progress in developing new rare earth materials for hole burning and coherent transient applications, *J. Lumin* **98**, 281 (2002).
- [16] S. P. Horvath, J. V. Rakonjac, Y.-H. Chen, J. J. Longdell, P. Goldner, J.-P. R. Wells, and M. F. Reid, Extending phenomenological crystal-field methods to C_1 point-group symmetry: Characterization of the optically excited hyperfine structure of $^{167}\text{Er}^{3+}:\text{Y}_2\text{SiO}_5$, *Phys. Rev. Lett.* **123**, 057401 (2019).
- [17] Y. Alizadeh, J. L. B. Martin, M. F. Reid, and J.-P. R. Wells, Intra- and inter-configurational electronic transitions of Ce^{3+} -doped Y_2SiO_5 : Spectroscopy and crystal field analysis, *Opt. Mater.* **117**, 111114 (2021).
- [18] S. P. Horvath, *High-resolution spectroscopy and novel crystal-field methods for rare-earth based quantum information processing*, Ph.D. thesis, University of Canterbury (2016).
- [19] X. Zhou, H. Liu, Z. He, B. Chen, and J. Wu, Investigation of the electronic structure and optical, epr, and odmr spectroscopic properties for $^{171}\text{Yb}^{3+}$ -doped Y_2SiO_5 crystal: A combined theoretical approach, *Inorg. Chem.* **59**, 13144 (2020), pMID: 32865403.
- [20] N. L. Jobbitt, S. J. Patchett, Y. Alizadeh, M. F. Reid, J.-P. R. Wells, S. P. Horvath, J. J. Longdell, A. Ferrier, and P. Goldner, Transferability of crystal-field parameters for rare-earth ions in Y_2SiO_5 tested by Zeeman spectroscopy, *Phys. Sol. State* **61**, 780 (2019).
- [21] N. L. Jobbitt, J.-P. R. Wells, M. F. Reid, and J. J. Longdell, Raman heterodyne determination of the magnetic anisotropy for the ground and optically excited states of Y_2SiO_5 doped with Sm^{3+} , *Phys. Rev. B* **103**, 205114 (2021).
- [22] S. Mothkuri, M. F. Reid, J.-P. R. Wells, E. Lafitte-Houssat, P. Goldner, and A. Ferrier, Electron-nuclear interactions as a test of crystal field parameters for low-symmetry systems: Zeeman hyperfine spectroscopy of Ho^{3+} -doped Y_2SiO_5 , *Phys. Rev. B* **103**, 104109 (2021).
- [23] J. L. Doualan, C. Labbe, P. L. Boulanger, J. Margerie, R. Moncorge, and H. Timonen, Energy levels of the laser active Er^{3+} ion in each of the two crystallographic sites of yttrium orthosilicate, *J. Phys. Condens. Matter* **7**, 5111 (1995).
- [24] Y. Sun, T. Böttger, C. Thiel, and R. Cone, Magnetic g tensors for the $^4\text{I}_{15/2}$ and $^4\text{I}_{13/2}$ states of $\text{Er}^{3+}:\text{Y}_2\text{SiO}_5$, *Phys. Rev. B* **77** (2008).
- [25] Y.-H. Chen, X. Fernandez-Gonzalvo, S. P. Horvath, J. V. Rakonjac, and J. J. Longdell, Hyperfine interactions of Er^{3+} ions in Y_2SiO_5 : Electron paramagnetic resonance in a tunable microwave cavity, *Phys. Rev. B* **97**, 024419 (2018).
- [26] B. A. Maksimov, V. V. Ilyukhin, Y. A. Kharitonov, and N. V. Belov, Crystal structure of yttrium oxyorthosilicate $\text{Y}_2\text{O}_3 \cdot \text{SiO}_2 = \text{Y}_2\text{SiO}_5$, *Kristallografiya* **15** (1970).
- [27] C. Li, C. Wyon, and R. Moncorge, Spectroscopic properties and fluorescence dynamics of $\text{Er}^{3+}:\text{Y}_2\text{SiO}_5$, *IEEE J. Quantum Electron.* **28**, 1209 (1992).
- [28] O. Guillot-Noël, P. Goldner, Y. L. Du, E. Baldit, P. Monnier, and K. Bencheikh, Hyperfine interaction of Er^{3+} ions in Y_2SiO_5 : An electron paramagnetic resonance spectroscopy study, *Phys. Rev. B* **74**, 214409 (2006).
- [29] G. Liu, *Spectroscopic properties of rare earths in optical materials*, edited by G. Liu and B. Jacquier (Springer Science & Business Media, 2006).
- [30] B. G. Wybourne, *Spectroscopic Properties of Rare Earths* (Interscience Publishers, 1965).
- [31] R. M. Macfarlane and R. M. Shelby, *Spectroscopy of Solids Containing Rare Earth Ions*, edited by A. A. Kaplyanskii and R. M. Macfarlane (North-Holland, Amsterdam, 1987).
- [32] D. J. Wales and J. P. K. Doye, Global optimization by basin-hopping and the lowest energy structures of Lennard-Jones clusters containing up to 110 atoms, *J. Phys. Chem. A* **101**, 5111 (1997).
- [33] D. J. Wales and H. A. Scheraga, Global optimization of clusters, crystals, and biomolecules, *Science* **285**, 1368 (1999).
- [34] N. Metropolis, A. W. Rosenbluth, M. N. Rosenbluth, A. H. Teller, and E. Teller, Equation of state calculations by fast computing machines, *J. Chem. Phys* **21**, 1087 (1953).

- [35] S. G. Johnson, The nlopt nonlinear-optimization package, <http://ab-initio.mit.edu/nlopt>.
- [36] R. C. Aster, B. Borchers, and C. H. Thurber, *Parameter estimation and inverse problems*, Vol. 90 (Academic Press, 2011).
- [37] W. T. Carnall, G. L. Goodman, K. Rajnak, and R. S. Rana, A systematic analysis of the spectra of the lanthanides doped into single crystal LaF_3 , *J. Chem. Phys.* **90**, 3443 (1989).
- [38] Y. Petit, B. Boulanger, J. Debray, and T. Chanelière, Demonstration of site-selective angular-resolved absorption spectroscopy of the ${}^4\text{I}_{15/2} \rightarrow {}^4\text{I}_{13/2}$ erbium transition in the monoclinic crystal Y_2SiO_5 , *Opt. Mater.: X* **8**, 100062 (2020).
- [39] Y. Y. Yeung, 'superposition model and its applications', in *Optical Properties of 3d-Ions in Crystals: Spectroscopy and Crystal Field Analysis*, edited by N. M. Avram and M. G. Brik (Springer Berlin Heidelberg, 2013).